Polarization modulation instability in a nonlinear fiber Kerr resonator

J. Fatome[1,*], B. Kibler[1], F. Leo[2], A. Bendahmane[1,3], G.-L. Oppo[4], B. Garbin[5], Y. Wang[5], S. G. Murdoch[5], M. Erkintalo[5] and S. Coen[5]

[1]*Laboratoire Interdisciplinaire Carnot de Bourgogne, UMR6303 CNRS-UBFC, Dijon, France.*
[2]*OPERA-Photonique, Université Libre de Bruxelles, CP 194/5, 50 Av. F. D. Roosevelt, B-1050 Brussels, Belgium.*
[3]*Now at Université Lille 1, IRCICA, Laboratoire PhLAM, 59655 Villeneuve d'Ascq, France.*
[4]*SUPA and Department of Physics, University of Strathclyde, Glasgow G4 0NG, Scotland, EU.*
[5]*Dodd-Walls Centre and Department of Physics, The University of Auckland, Private Bag 92019, Auckland 1142, New Zealand.*
**Corresponding author: Julien.Fatome@u-bourgogne.fr*

Received XX Month XXXX; revised XX Month, XXXX; accepted XX Month XXXX; posted XX Month XXXX (Doc. ID XXXXX); published XX Month XXXX

We report on the experimental and numerical observation of a polarization modulational instability (PMI) process occurring in a nonlinear fiber Kerr resonator. This phenomenon originates from the phase detuning between both principal modes of polarization circulating within the cavity due to its intrinsic birefringence as well as their nonlinear coupling through cross-phase modulation (XPM). Our experimental investigation is based on a 10-m-long fiber ring cavity in which a polarization controller is inserted to finely control the level of birefringence imposed in the resonator. Depending on this amount of birefringence, both single-round trip (P1) and two-round trips (P2) periodic behaviors can be observed. Experimental results are well confirmed by theoretical predictions of PMI gain bands and numerical simulations based on two coupled Ikeda maps for both orthogonally polarized modes. Our study provides new insights into the control of MI into birefringent Kerr resonators and related frequency comb generation.

OCIS codes: *(190.4370) Nonlinear optics, fibers; (140.4780) Optical resonators; (260.5430) Polarization.*

http://dx.doi.org/10.1364/OL.99.099999

Modulation instability (MI) is a nonlinear phenomenon occurring in Kerr media for which weak perturbations resting onto an intense continuous-wave (cw) landscape experience an exponential growth owing to a parametric gain [1-2]. In anomalous dispersive optical fibers, MI occurs due to a perfect balance between chromatic dispersion and Kerr nonlinearity, leading to a large transfer of energy from the central cw pump into two spectral MI sidebands [1-2]. In the case of coherently-driven dissipative Kerr resonators, such as fiber ring cavities, it has been shown that the specific boundary conditions imposed on the cavity also play a crucial role in the phase matching condition leading to emergence of MI [3-5]. So far, several kinds of MI regimes and pumping configurations of fiber cavities have been reported in the literature including MI in anomalous and normal dispersion regimes, bichromatic pumping configuration, Faraday MI, incoherent pumping, period-doubled (P2) behavior and so on [6-11]. In the temporal domain the MI process in Kerr resonators leads to the emergence of periodic patterns which are fundamentally related to the existence of cavity solitons and related optical frequency combs in microresonators [12-15].

Less studied in coherently driven passive cavities, is the vectorial counter-part of this process, associated to fiber birefringence and known as polarization modulational instability (PMI). Indeed, the additional degree of freedom offered by birefringence as well as the nonlinear coupling between the polarization components of light through XPM can also fulfill phase-matching conditions thus enabling the manifestation of PMI and emergence of vectorial temporal patterns [16-21].

In the present contribution, we report on the experimental observation of a polarization modulation instability process occurring in a fiber Kerr resonator. Our experimental test-bed platform is based on a 10-m long normally dispersive spun-fiber ring cavity including a polarization controller that enables the careful adjustment of its birefringence. This induced-birefringence impacts on the phase detuning between both orthogonally polarized principal modes of the cavity which in turn imposes the frequency of the PMI sidebands. Moreover, we found that this amount of phase detuning can lead to single-round trip behavior (P1) or period-doubled dynamics occurring on a two-round trips cycle (P2). Experimental results are in good agreement with theoretical predictions and numerical simulations based on an iterative resolution of coupled Ikeda maps.

The experimental setup is displayed in Fig. 1(a). Basically, it consists of a passive fiber ring cavity made of a close loop of L = 10-m long normally dispersive spun fiber provided by Ixblue Photonics. The fiber undertest is characterized by a chromatic dispersion parameter D = –44 ps/nm/km and a Kerr parameter γ = 6.5 $W^{-1}.km^{-1}$. It is important to notice that the fiber was specifically designed to reduce the residual birefringence by means of a fast spinning of the preform imposed during the drawing stage of the manufacturing process (spatial period of 5 mm). With such a process, any residual geometrical defect or anisotropy can be canceled out in such a way to consider the fiber segment as an isotropic-like fiber ring. Furthermore, in order to prevent any additional source of residual birefringence, the fiber was carefully off-spooled and wound directly on our experimental board with a diameter close to 50 cm. Consequently, the birefringence induced by fiber-bending was estimated around Δn<10^{-8} [22], and can thus be neglected in our experiments.

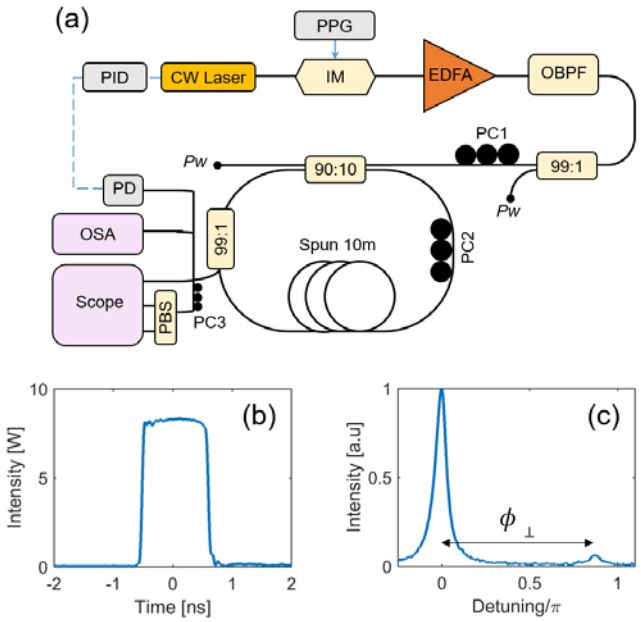

Fig. 1. (a) Experimental setup. PPG: pulse pattern generator, IM: intensity modulator, PC: polarization controller, EDFA: Erbium doped fiber amplifier, OBPF: optical bandpass filter, PBS: Polarization beam splitter, OSA: optical spectrum analyzer, PID: proportional integral derivative system, PD: photodetector, Pw: power-meter. (b) Input pulse profile. (c) Linear resonance of the cavity.

Our fiber cavity is pumped thanks to a continuous wave (CW) laser centered at 1552.4 nm (linewidth <1 kHz). The cw pump beam is then intensity-modulated to generate 1.1-ns square pulses, see Fig. 1(b), at a repetition rate of 17.54 MHz (corresponding to one cavity round-trip time). This intensity modulation stage simultaneously enables the increase of pump peak power and the circumvention of Brillouin backscattering within the cavity. The pulsed pump is then amplified by means of an Erbium-doped fiber amplifier (EDFA) and injected into the cavity. At each round-trip, the coherent driving pump is superimposed to the circulating signal thanks to a 10:90 coupler (θ = 0.1) made of standard single mode fiber (SMF). A 99:1 SMF tap-coupler is also added to extract a part of the intra-cavity field. For that configuration, the cavity finesse was measured to be about F=27. The linear detuning seen by the pump wave at each round-trip (ϕ_0) is stabilized thanks to a proportional integral derivative (PID) system that finely adjusts the laser wavelength with respect to the nonlinear cavity resonance. At the output of the cavity, temporal, polarization and spectral characterizations of PMI are provided by means of an optical spectrum analyzer (OSA) and a real-time 50-GHz bandwidth oscilloscope coupled to a polarization beam splitter (PBS) and two fast photodetectors.

Polarization management of this experiment is achieved by means of three polarization controllers (PC). First, a careful control of the input polarization state is ensured via PC1 in order to principally excite one of the principal SOP of the fiber ring. A second inner polarization controller (PC2) is implemented directly onto the spun fiber so as to finely control the level of birefringence of the cavity through mechanical stress. In this way, the phase detuning between both principal SOPs of the cavity $\phi_\perp$ can be carefully adjusted between $-\pi$ and π and moreover, can be directly monitored from measurement of both linear resonances, see Fig. 1(c). Finally, a third polarization controller (PC3), inserted in the output of the system enables us to select the orthogonal polarization basis for spectral and temporal characterizations.

The modelling of our vectorial Kerr resonator is based on the integration of the following coupled Ikeda maps for which u and v correspond to the right- and left-handed circular polarization components of the intracavity field at the n^{th} round-trip. Since the fiber is supposed isotropic, this map is constructed by combining the usual system of two coupled nonlinear Schrödinger equations (Eqs. (1)), describing the evolution of the field envelope within an isotropic fiber, together with boundary conditions (Eqs. (2) and (3)) that relate the fields between successive round-trips and the input pump expressed in the circular basis (u_{in} and v_{in}).

$$\begin{cases} i\frac{\partial u}{\partial z} = \frac{\beta_2}{2}\frac{\partial^2 u}{\partial t^2} - \gamma'(|u|^2 + 2|v|^2)u \\ i\frac{\partial v}{\partial z} = \frac{\beta_2}{2}\frac{\partial^2 v}{\partial t^2} - \gamma'(|v|^2 + 2|u|^2)v \end{cases} \quad \textbf{(1)}$$

$$\begin{pmatrix} u \\ v \end{pmatrix}^{n+1} = (1-\alpha)exp\left(i\left[\phi_0 + \frac{\phi_\perp}{2}\right]\right)\begin{pmatrix} u \\ v \end{pmatrix}^{n} M + \sqrt{\theta}\begin{pmatrix} u_{in} \\ v_{in} \end{pmatrix} \quad \textbf{(2)}$$

with

$$M = \begin{bmatrix} cos(\phi_\perp/2) & -i\,sin(\phi_\perp/2) \\ -i\,sin(\phi_\perp/2) & cos(\phi_\perp/2) \end{bmatrix} \quad \textbf{(3)}$$

Here, z represents the propagation distance within the cavity and t the time in a delayed reference frame, β_2 is the second-order chromatic dispersion coefficient, γ'=2/3γ. $\alpha = \pi/F = 0.11$ represents half of the total loss of the cavity, while ϕ_0 is related to the cavity detuning coefficient $\Delta = (2k\pi - \phi_0)/\alpha$. As mentioned above, $\phi_\perp$ denotes the birefringence and represents the phase shift difference accumulated over one round-trip between the principal polarization modes of the cavity (supposed here as linear). Finally, we suppose a linear polarization external pumping, meaning that all the energy provided by the pump to the system is contained in one principal polarization mode of the cavity. That is to say, both circular components u_{in} and v_{in} are evenly excited at the input of the cavity.

In order to highlight the key role of the intra-cavity birefringence in the PMI process, we have first numerically solved the vectorial Ikeda maps described above and depicted the resulting steady-state spectrum of the cavity with respect to the birefringence detuning $\phi_\perp$. Results are summarized in Fig. 2(a) for a pump peak power of 8

W, a linear detuning Δ=7, as well as a finite extinction-ratio between both linear components of the pump beam of 30 dB. From Fig. 2(a), we can see the appearance of an intra-cavity modulational instability process with the generation of several harmonic frequencies around the pump wavelength. We can notice that the characteristic "umbrella-shape" of these maps is pretty well symmetrical for detuning values of $\phi_\perp$ modulo $k\pi$ and that no PMI was observed for birefringence detuning between $0 < \phi_\perp < 0.3\pi$ and $-\pi < \phi_\perp < -0.7\pi$. Moreover, as expected, the optimum frequency of the PMI process is found to dramatically depend on the phase detuning between both principal SOPs of the cavity. This frequency (Ω) can be approximated by the following phase-matching condition, represented with circles in Fig. 2(a) and taking into account for the balance between chromatic dispersion, linear detuning, birefringence and intra-cavity nonlinearity (P):

$$\Omega^2 \frac{\beta_2 L}{2} + (\phi_\perp - \Delta\alpha) + \gamma' P L = k\pi \qquad \textbf{(4)}$$

Fig. 2(b) depicts the corresponding concatenated experimental spectra recorded at the output of the cavity as a function of the intra-cavity birefringence $\phi_\perp$, here adjusted by means of the inner polarization controller (PC2). The input pump peak power is estimated to be 8 W while the linear detuning is kept constant to Δ=7. We can observe a good qualitative agreement with our previous numerical simulations of Fig. 2(a) and in particular the typical "umbrella-shape" mapping of this process characterized by the emergence of well separated, far detuned and thin sidebands corresponding to PMI frequencies.

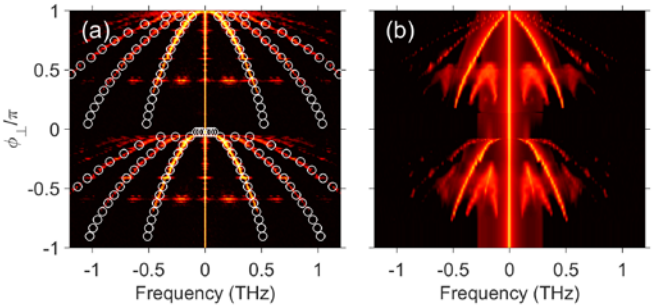

Fig. 2. Pseudo-color plots reporting the evolution of the output spectrum according to the birefringence detuning $\phi_\perp$. (a) Numerical results are compared with theoretical predictions of Eq. (4) in circles. (b) Corresponding experimental results. In both cases, the input peak-power was fixed to P=8 W and the linear detuning is kept constant to Δ=7. Data values are normalized with respect to the pump power.

To summarize and fairly compare the different results obtained from numerical simulations, experiments and theoretical predictions, we have reported in Fig. 3(a) the frequencies of the first-order PMI sidebands as a function of the birefringence detuning $\phi_\perp$. Note that several experimental series have been concatenated so as to sweep the whole birefringence range. We can then observe a pretty good agreement between our measurements (circles), numerical results (stars) and phase-matching condition (dashed-line).

In order to further assess the vectorial nature of the observed PMI process, we have recorded the output spectrum projected along an orthogonal linear basis corresponding to the pump SOP and its orthogonal component. The results are reported in Fig. 3(b) for a birefringence detuning $\phi_\perp$=0.85π. They clearly show that the first MI sidebands are mainly generated orthogonally to the pump wave with an extinction-ratio above 20 dB and then alternate between both SOPs for the higher-order sidebands. Note that this behavior is similar to the general case observed in conventional isotropic PMI experiments performed in straight-line single-pass fiber segments [23].

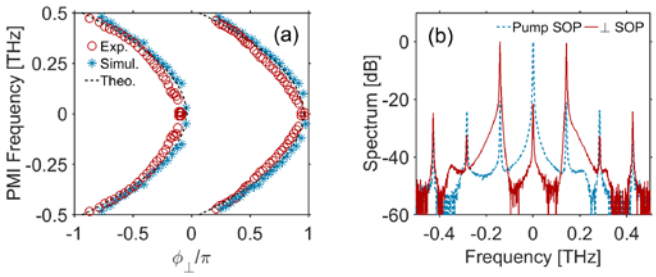

Fig. 3. (a) Optimum PMI frequency (Ω) for the first-order sideband as a function of the birefringence detuning $\phi_\perp$. Experimental results (circles) are compared with numerical simulations (stars) as well as theoretical predictions of Eq. (4) (dashed-line). In all cases, the input peak-power is fixed to 8 W and the linear detuning is kept constant to Δ=7. (b) Output spectrum for $\phi_\perp$=0.85π recorded behind the output PBS and decomposed in an orthogonal basis corresponding to the pump SOP and its orthogonal component.

In addition to the spectral analysis shown in Figs. 2&3, we have also performed a temporal characterization of the intra-cavity field by means of a 50-GHz bandwidth real-time oscilloscope. To this aim, owing to the inner polarization controller PC3, the birefringence of the cavity $\phi_\perp$ was finely adjusted close to 0 and then π so as to generate a periodic MI pattern in accordance to the bandwidth of our 50-GHz photodetectors. We have then monitored the corresponding temporal profile at the output of the PBS. The output polarization basis was then carefully adjusted in such a way to maximize the contrast of the oscillations between both orthogonal polarization components. Note that from a theoretical point of view, this basis is supposed to be the right- and left- circular components of the intra-cavity field. In practice, however, the principal SOPs of the cavity are doubtless elliptical instead of perfectly linear and thus the output polarization basis remains arbitrary selected.

Figure 4 illustrates a typical experimental intensity profile recorded for $\phi_\perp \sim 0$ beyond the PBS when the polarization basis is optimized thanks to PC3. We can then observe large temporal oscillations at a repetition rate of 15 GHz as well as a perfect anti-correlation between both orthogonal polarization components, as expected from vectorial MI process [16, 17, 23].

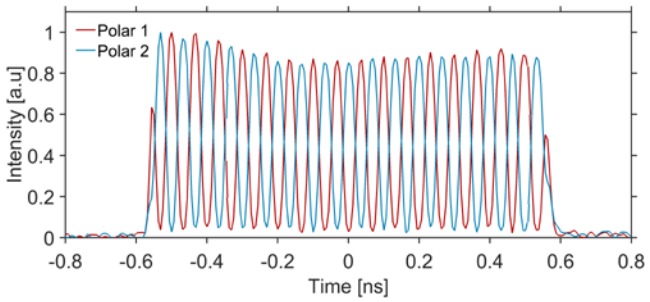

Fig. 4. Typical experimental intensity profiles of both orthogonal components monitored at the output of the cavity obtained for $\phi_\perp \sim 0$.

The temporal evolution of the PMI process is even more interesting when monitored as a function of circulating round-trips. To this aim, single-shot data sequences recorded on a long temporal window have been acquired on our oscilloscope so as to reconstruct the evolution of the intra-cavity field with respect to successive round-trips. Figure 5(a) displays the evolution of a polarization component recorded for $\phi_\perp \sim 0$. We can observe a steady-state evolution with a constant periodic MI pattern recirculating into the cavity with one round-trip period (P1 behavior). Note here the typical polarization nature of this PMI process for which the total intensity profile, shown in Fig. 5(b), remains perfectly constant along the propagation. The modulated pattern is only visible in the polarization domain. Figures 5(c&d) display the results obtained for a birefringence detuning close to π. In this case, as can be seen in the checkerboard-like mapping of Fig. 5(c), the anti-resonant phase matching condition leads to a period-doubled P2 behavior for which the PMI pattern switches between both polarization components at each round-trip [18]. This behavior can be simply understood by the fact that the π-phase-shift imposed at each round-trip on both principal polarization modes of the cavity and due to residual birefringence makes the fiber ring acting as a half-wave-plate. Consequently, this half-wave-plate process makes swap the light's handedness on a two-round-trips period, and gives rise to the flipping of the PMI pattern. Finally, note that similarly to the previous case, the total intensity profile in Fig. 5(d) remains constant, thus concealing the polarization information.

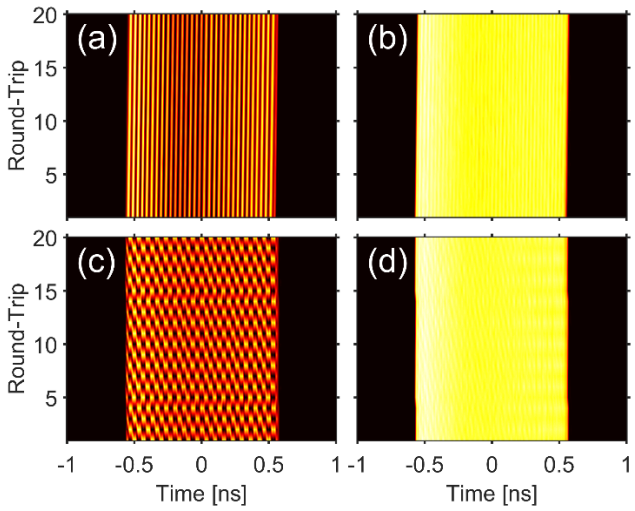

Fig. 5. (a) Experimental evolution of the intensity profile monitored on one polarization component as a function of round-trips for $\phi_\perp \sim 0$ (b) Corresponding total intensity profile (before PBS). (c & d) Same as (a& b) but with $\phi_\perp$ close to π.

In conclusion, we have reported the first experimental observation of polarization modulational instability in a fiber Kerr resonator. It was shown that the optimum PMI frequency is directly related to the level of the intrinsic birefringence present in the resonator and can be well approximated through a phase-matching condition taking into account for this polarization phase detuning. Our experimental observation were performed thanks to a 10-m long spun fiber ring cavity for which an inner polarization controller enables us to precisely control its the level of birefringence. By means of real-time temporal characterizations, both single-round trip (P1) and period-doubled (P2) behaviors have been highlighted. Experimental results were found to be in good agreement with theoretical predictions and numerical simulations based on coupled Ikeda maps. Finally, these results provide new insights into the control of dissipative MI into birefringent Kerr resonators as well as a potential new degree of freedom for frequency comb generation.

Funding. J. F. acknowledges the financial support from the Conseil Régional de Bourgogne Franche-Comté, APEX project and International Mobility Program as well as fonds européen de développement regional (FEDER), Quasimir project. B. K. acknowledges support from the French program Investissements d'Avenir (Project No. PIA2/ISITE-BFC, contract n° ANR-15-IDEX-03).

Acknowledgment. We thank Dr. Pierre Béjot for fruitful discussions.

References

1. K. Tai, A. Hasegawa, and A. Tomita, Phys. Rev. Lett. **56**, 135 (1986)
2. G. P. Agrawal, *Nonlinear Fiber Optics* (5th ed., Academic Press, Oxford, 2013).
3. M. Nakazawa, K. Suzuki, and H. A. Haus, Phys. Rev. A **38**, 5193 (1988).
4. R. Vallée, Opt. Commun. **81**, 419 (1991).
5. M. Haeltermann, S. Trillo, and S. Wabnitz, Opt. Commun. **91**, 401 (1992).
6. S. Coen and M. Haelterman, Phys. Rev. Lett. **79**, 4139 (1997).
7. F. Copie, M. Conforti, A. Kudlinski, A. Mussot, and S. Trillo, Phys. Rev. Lett. **116**, 143901 (2016).
8. D. Ceoldo, A. Bendahmane, J. Fatome, G. Millot, T. Hansson, D. Modotto, S. Wabnitz, and B. Kibler, Opt. Lett. **41**, 5462 (2016).
9. M. Conforti, A. Mussot, J. Fatome, A. Picozzi, S. Pitois, C. Finot, M. Haelterman, B. Kibler, C. Michel, and G. Millot, Phys. Rev. A **91**, 023823 (2015).
10. A. Bendahmane, J. Fatome, C. Finot, G. Millot, and B. Kibler, Opt. Lett. **42**, 251 (2017).
11. T. Hansson and S. Wabnitz, J. Opt. Soc. Am. B **32**, 1259 (2015).
12. S. Coen and M. Haelterman, Opt. Lett. **26**, 39 (2001).
13. F. Leo, S. Coen, P. Kockaert, S. P. Gorza, P. Emplit, and M. Haelterman, Nat. Photon. 4, 471-476 (2010).
14. A. A. Savchenkov, A. B. Matsko, and L. Maleki, Nanophoton. **5**, 363 (2016).
15. P. Del'Haye, A. Schliesser, O. Arcizet, T. Wilken, R. Holzwarth, and T. J. Kippenberg, Nature **450**, 1214 (2007).
16. A. L. Berkhoer, and V. E. Zakharov, Sov. Phys. JETP **31**, 486 (1970).
17. M. Haelterman , S. Trillo, and S. Wabnitz, JOSA B **11**, 446 (1994).
18. M. Haelterman and M. D. Tolley, Opt. Commun. **108**, 167 (1994).
19. I. P. Areshev, T. A. Murina, N. N. Rosanov and V. K. Subashiev, Opt. Commun. **47**, 414 (1983).
20. A. Tonello, Opt. Quant. Electron. **32**, 1219-1238 (2000).
21. T. Hansson, M. Bernard, and S. Wabnitz, J. Opt. Soc. Am. B **35**, 835 (2018).
22. L. Palmieri, A. Galtarossa, and T. Geisler, Opt. Lett. **35**, 2481 (2010).
23. P. Kockaert, M. Haelterman, S. Pitois, and G. Millot, Appl. Phys. Lett. **75**, 2873 (1999).